

THE PENNSYLVANIA STATE UNIVERSITY
SCHREYER HONORS COLLEGE

DEPARTMENT OF BIOENGINEERING

A COMPUTATIONAL STUDY OF AIRFLOW IN A STANDARDIZED HUMAN NASAL
CAVITY: IMPLICATIONS REGARDING OLFACTION

ELIZABETH M. SHENK

Spring 2010

A thesis
submitted in partial fulfillment
of the requirements
for a baccalaureate degree
in Bioengineering
with honors in Bioengineering

Reviewed and approved* by the following:

Brent A. Craven
Research Associate, Applied Research Lab
Thesis Supervisor

William O. Hancock
Associate Professor in Bioengineering
Honors Adviser

Peter J. Butler
Associate Professor in Bioengineering

* Signatures are on file in the Schreyer Honors College.

Abstract

Healthy humans breathe through their nose even though its complex geometry imposes a significantly higher resistance in comparison with mouth breathing. The nose serves many functions, the focus of which in this thesis is olfaction. Sniffing is typically considered to enhance the sense of smell; the flow rate through the human nasal cavity during sniffing is significantly higher than that which is experienced during restful breathing. This study uses a standardized three-dimensional model of the human nasal cavity and computational fluid dynamics to study the physiology and fluid dynamics of human respiration and olfaction during sniffing. The flow is modeled as quasi-steady and laminar due to Womersley and Reynolds number calculations. The qualitative features of the CFD solutions are fairly consistent for the coarse, medium, and fine grids. The overall flow patterns are remarkably similar regardless of the refinement of the grid; however there are marked differences in the flow rates and velocity profiles as the grid refinement progresses from coarse to medium to fine. The olfactory region of the human nasal cavity experiences a relatively low velocity of airflow, as well as a relatively low fraction of the airflow through the nasal cavity in this simulation. The high flow rate (40 L/min) simulated as the human sniffing flow rate did not appear to facilitate transport of odorant molecules into the olfactory region. Overall, the results from this study do not appear to show any significant benefits to human olfactory ability during sniffing.

Table of Contents

Section	Page Number
1.0 Introduction	1
1.1 Anatomy of the Nose	1
1.2 Functions of the Nose	4
1.3 Nasal Airflow	5
1.4 Olfaction	7
1.4.1 Olfactory Airflow	9
1.4.2 Implications of Olfactory Airflow	10
1.4.3 Effects of Sniffing on Olfaction	11
1.5 Objective	12
2.0 Computational Methodology	13
2.1 Standardized Nasal Cavity Geometry	13
2.2 Assumptions	14
2.3 Boundary Conditions	15
2.4 Grid Generation	16
2.5 Numerical Methods	18
3.0 Results and Discussion	19
4.0 Conclusions	34
4.1 Future Work	35
References	36
Acknowledgments	38

1.0 Introduction

Healthy humans normally breathe through their nose, even though its complex anatomy imposes a significantly higher airflow resistance in comparison with mouth breathing. The nose serves many functions, the focus of which in this thesis is olfaction. In the study of olfaction, many functional aspects of the nose must be considered, particularly related to intranasal airflow phenomena.

1.1 Anatomy of the Nose

The nasal cavity is bilaterally-symmetric and is separated into two airways by the nasal septum. Air enters each nasal airway through an oval-shaped external opening called the naris or nostril. Just beyond the external naris is a funnel-shaped dilated region called the vestibule. The narrow end of the vestibule leads to a region referred to as the nasal valve, where the airway constricts to a narrow slit and bends approximately 90 degrees toward the horizontal. Caudal to the nasal valve, the cross-sectional area of the airway increases, and the region referred to as the “main nasal passage” begins. The main nasal passage extends about 5 cm to the posterior end of the cavity. The airways are 1-3 mm wide in this region, and the distance between the nasal roof and floor is approximately 4 cm (Keyhani et al., 1995). The roof of the nasal cavity is formed by bones and cartilage while the floor is formed by the palate, which separates the nasal and oral cavities and extends horizontally toward the back of the skull (Liu et al., 2009).

The main nasal passage can be subdivided into different parts. On the lateral wall there are three wing-like projections: the superior, middle, and inferior turbinates that serve to increase the surface area exposed to the air, thus augmenting heat and moisture exchange. The airways inferior and lateral to the turbinates are referred to as meatuses; each meatus is named for the turbinate that lies above it (Keyhani et al., 1995). The anatomy of the human nasal cavity can be seen in Figure 1. The slit-shaped region medial to the superior turbinate is the olfactory airway, the definition of the olfactory region can be seen in Figure 2; the surface of the olfactory airway is covered with olfactory epithelium. The remainder of the nose is predominantly lined with respiratory mucosa, which clears the nasal cavity of inhaled noxious substances via mucociliary transport whereby contaminated mucus is propelled towards the pharynx where it is swallowed.

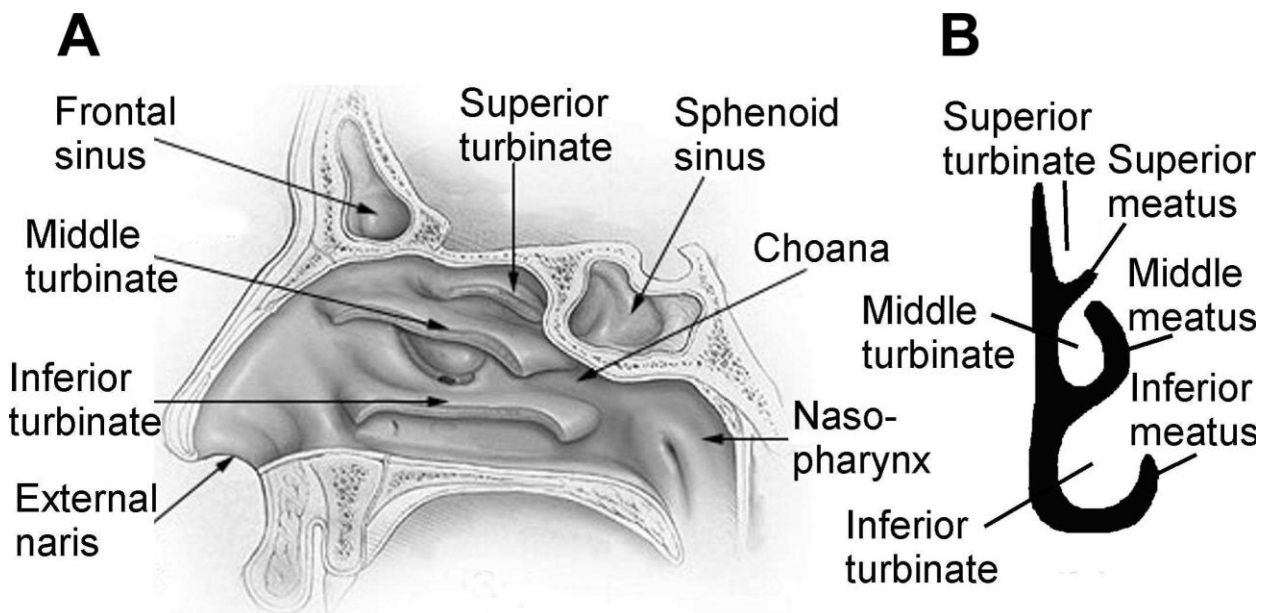


Figure 1: Anatomy of the human nose (Liu et al., 2009).

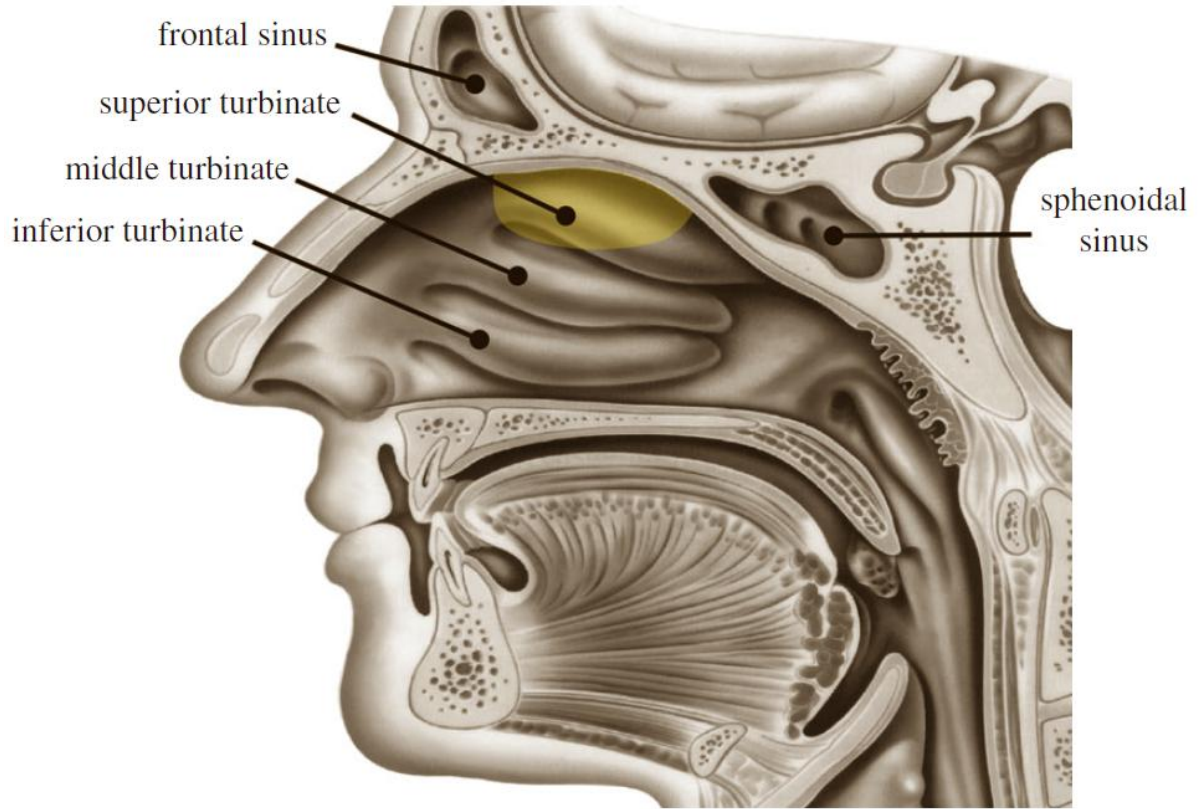


Figure 2: Location of the olfactory receptor cells, yellow, in the human nasal cavity anatomy (Hornung, 2006) (Lang, 1989) (Craven et al., 2009).

Although the main anatomical characteristics of the human nose are similar from one individual to the next, there are distinct intraspecific differences in nasal anatomy. Externally, there is variability in the length and width of the nostrils as well as the nostril angle (defined as the angle of the entry plane between the major axis of the nostril and the base of the nose). Internally, differences can exist between the left and right cavities of an individual as a result of periodic alteration in nasal patency of the left and right airways and deformities such as a deviated septum (Zhao et al., 2004).

A few studies have addressed the anatomical differences between human nasal passages. Zhao et al. (2004) used CT scans for one patient and observed significant differences

between the two airways of that one person. Additionally, Liu et al. (2009) analyzed 30 sets of CT scans of human nasal passages. Each of the nasal cavities was slightly different from the rest and from this data set a standardized nasal passage was computed. A standardized model of the human nasal passages is extremely important as it is representative of the general population's nasal cavities. Consequently, this standardized model can be used as a reference in clinical settings to diagnose unhealthy patients and as a standard for computational modeling (e.g., fluid dynamics and odorant deposition) (Liu et al., 2009). This paper addresses the latter benefit of the standardized model by exploring the airflow patterns through the model during sniffing.

1.2 Functions of the Nose

The nose is a complex structure that has three basic functional roles. First, defense – the nose acts as a filter, trapping vapor and particles in the mucus lining. Second, air conditioning – the nasal airway warms and humidifies inspired air to nearly alveolar conditions to protect the alveolar lining where gas exchange occurs. Third, olfaction – the nose provides the sense of smell, whereby odorant molecules interact with olfactory receptors located in the superior part of the nasal cavity (see Figure 1, Elad et al., 2008). All three of these basic physiological functions rely on the thin mucus layer that lines the nasal airway. Specifically, nasal secretions augment heat transfer, humidify inspired air, dehumidify expired air, provide an effective barrier between inhaled noxious chemicals and underlying tissue, absorb odorant molecules, and aid in the removal of inspired particles by means of mucociliary transport (Craven et al., 2007).

1.3 Nasal Airflow

Animals with a characteristic body size greater than approximately 1 mm rely on convective transport phenomena for respiration and olfaction (Doorly et al., 2008). The effectiveness of convective transport depends on the fluid dynamics, which is characterized by the Reynolds number, the ratio of inertial to viscous forces in the fluid flow. Airflow in the human nasal cavity is inertially dominated. In our model, the Reynolds number reaches a peak value around 2000, within the laminar flow regime.

In general, when a healthy human breathes through their nose, inhaled air enters the nostril and passes through the narrowest portion of the nasal cavity (i.e., the nasal valve) where it accelerates (Liu et al., 2009). The air then expands into a much wider passageway, the middle and posterior part of the nasal cavity. There, the air decelerates in order to maintain a constant flow rate while it circumvents the three turbinates.

Nasal airflow patterns have been shown to be independent of the flow rate (Keyhani et al., 1995). Generally, the flow is laminar when the half-nasal flow rates are below 200 ml/s, such as during quiet breathing. At much higher flow rates, the flow becomes unstable during more forceful breathing and turbulent regions may appear (Keyhani et al., 1995). The half-nasal flow rate in this thesis is set to be about 650 ml/s, which is the maximum airflow rate during sniffing (Hornung, 2006).

Within the nasal cavity, airflow can be described as having three distinct flow paths. One portion of air flows through the inferior meatus and other inferior portions of the airway, close to the nasal floor; this is known as the ventral stream. A second portion of air flows through the lateral portions of the meatuses; this stream is called the lateral stream. The final portion of air flows through the upper portions of the nasal cavity, including the olfactory region; this stream is the dorsal stream, and generally consists of the lowest flow rates (Subramaniam et al., 1998).

A few important flow features have previously been identified. First, the highest velocities occur in the nasal valve and the inferior airway. This is logical considering that the smallest cross-sectional area in the nasal cavity occurs in the nasal valve (Kelly et al., 2000). Thus, in order for the flow rate to remain constant, the velocity must increase in this area. Additionally, the inferior airway seems to provide the path of least resistance for air that is exiting the nasal valve, which explains the high flow rate in the inferior airway. The second important flow feature is very little flow in the meatuses. Finally, there is only a small fraction of airflow in the olfactory slit (about 5-15%) (Keyhani et al., 1997) (Hahn et al., 1993) (Taylor et al., 2009). It has been proposed that this region of low-flow is a defense mechanism “that prevents particles whose trajectories are heavily dependent on flow patterns from being convected to and deposited on the sensitive olfactory nerve fibers, while allowing vapors to diffuse to that region for olfaction” (Kelly et al., 2000).

1.4 Olfaction

Olfactory receptors, located beneath a thin mucus layer on the olfactory epithelium, detect odors when chemical molecules are transported through the nasal cavity. In general, macrosmats (excellent smelling animals such as the dog) have an “olfactory recess” (Craven et al., 2009) located near the back of the nasal cavity, which is absent in microsmats such as the human. Factors that most significantly affect the amount of odorant deposition in the olfactory mucosa include solubility of the odorant in mucus and the nasal airflow rate (Zhao and Dalton, 2007).

Generally, it is believed that humans have an inferior sense of smell compared to animals such as the dog. Some recent studies have shown that humans have a significantly smaller number of functional olfactory receptor genes than the primates from which they evolved (Shepherd, 2004). There are also evolutionary arguments that support this hypothesis: as humans evolved, the nose became smaller, and farther away from the ground as an erect posture developed. Additionally, the eyes moved closer to one another in the middle of the face – which increases the ability of depth vision. Despite these arguments for humans having a relatively poor sense of smell, studies have also been performed recently that indicate humans may actually have a relatively good sense of smell, since they have apparent advantages in the areas of nasal cavity structure, retronasal smell, and olfactory brain areas that outweigh the disadvantage of a lower number of olfactory receptors (Shepherd, 2004).

There is a reduction in the proportion of functional olfactory receptor genes from rodents to humans. Mice have approximately 1100 functional olfactory reception genes out of 1300 total, while humans have only 350 functional olfactory reception genes out of a total of approximately 1000 (Glusman et al., 2001) (Zozulya et al., 2001). Consequently, it has been concluded that the small number and proportion of functional olfactory receptor genes in humans directly correlates with the relatively poor human sense of smell. However, behavioral studies have been refuting this direct correlation. For example, Bisulco and Slotnick (2003) have shown that the removal of 80% of the glomerular layer in the rat does not significantly affect its olfactory detection and discrimination. These results suggest that the number and proportion of functional olfactory genes cannot directly correlate to a diminished sense of smell. Therefore, the fluid dynamics within the olfactory region of the nasal cavity as well as odorant deposition is likely the key to olfactory acuity.

Other studies have compared data on odor detection thresholds. In these studies, humans have performed not only as well or better than primates, but also arguably as well or better than other mammals. For example, when dogs, humans, and rats were tested for thresholds to the odors of straight-chain aldehydes, humans performed significantly better than rats, and although dogs perform at a level superior to humans on short chain compounds, humans perform at a level superior to dogs when tested on long chain compounds (Laska et al., 2000). These results have been replicated for other types of odors as well. Furthermore, humans have outperformed sensitive measuring instruments such as the gas chromatograph in tests of odor detection. Taken together, these results suggest that humans may actually be relatively good smellers, not the relatively poor smellers they are thought to be.

Humans are also not limited to the orthonasal route of smelling; retronasal smelling may actually give humans a slight advantage over other animals in certain tasks (Shepherd, 2004). By transporting odor molecules to olfactory receptor cells from the back of the oral cavity, the retronasal route of smelling allows for humans to perceive the odors of the foods and liquids which are within our mouths. Additionally, the higher brain functions that humans possess aid in olfaction. Many regions of the brain process odor input and aid in smell detection and smell discrimination. In summary, the results from all of these studies generally indicate that the number of olfactory receptor genes most likely does not have a direct relationship with olfactory acuity and that humans have a better sense of smell than is generally believed.

1.4.1 Olfactory Airflow

The volume of airflow passing through the olfactory system is affected by flow separation that may occur in both olfactory and respiratory regions of the nose (Keyhani et al., 1997). Overall, only about one-tenth of the total airflow that passes through the nasal cavity ever reaches the olfactory region of the respiratory system. This air normally enters through the anterior tip of the naris, especially during the laminar flow of restful breathing (half-nasal flow rates between 125 ml/s and 200 ml/s) (Keyhani et al., 1995).

Several parameters have been shown to affect the local olfactory odorant flux at a given flow rate. These include the nasal airway geometry and the thickness of the mucus lining

(Keyhani et al., 1997). Additionally, the width of the olfactory slit can have an impact on olfactory flux, depending on the solubility of the odorant. Odorants that have a higher mucosal solubility are affected much more by anatomical changes of the airway (and the corresponding local airflow pattern) than odorants that have a low mucosal solubility.

The human nasal cavity does not possess an olfactory recess as does the canine and rat nose. This leads to a nasal airflow pattern in the human that is extremely different from the canine and rat. Since the human olfactory region is located within the main respiratory flow path, when humans expire, the odorants in the olfactory region are removed, and new odorants are able to be detected through the retronasal route. This does not happen in the canine due to an overall nasal airflow pattern that prevents access to the olfactory recess via the retronasal route (Craven et al., 2009). The act of sniffing in humans can even yield airflow patterns that are different within the two cavities of the same subject. The use of a standardized model of the nasal cavity will provide a general description of the fluid dynamics within the “average” human nose.

1.4.2 Implications of Olfactory Airflow

To understand human olfaction it is important to have knowledge of the airflow and odorant transport patterns in the nasal cavity. The continuity, Navier-Stokes, and species transport equations govern the transport of odorant molecules. Different odorants have different mucus solubilities, which affects the odorant uptake over the olfactory mucosal surface (Keyhani et al., 1997). An increase in flow rate causes odorants with high mucosal

solubilities to increase their olfactory flux, while those odorants with low mucosal solubilities suffer a decrease in olfactory flux with an increase in flow rate. As one might expect, odorants with intermediate mucosal solubilities have an intermediate response, displaying very little change in overall olfactory flux with an alteration of the airflow rate.

1.4.3 Effects of Sniffing on Olfaction

Many animals, including humans, sniff to enhance their olfactory performance. There is an interest in the intranasal fluid dynamics during sniffing for a number of reasons – including a diagnostic and therapeutic viewpoint. In humans, mild sniffing consists of “short sequential bursts of high inspiratory airflow rate (>500 ml/s through each nostril) without exhalation in between” (Doorly et al., 2008). The increased pressure drop associated with mild sniffing causes a small degree of collapse of the external nose, affecting internal airflow in the nasal cavity. Deep sniffing, however, causes an even larger pressure drop and a higher flow rate (between 600 and 1000 ml/s through each nostril) that may result in turbulent flow, assisting transport to the olfactory region. It has been proposed that sniffing causes significantly more air to flow through the olfactory region, increasing olfactory ability (Zhao et al., 2006). This study investigates deep sniffing in order to analyze whether deep sniffing really does enhance odorant transport to the olfactory region of the human nasal cavity.

1.5 Objective

The objective of this study is to use a standardized three-dimensional model of the human nasal cavity to study the fluid dynamics of human respiration and olfaction. Computational fluid dynamics will be used to simulate nasal airflow to better understand the physiology of respiration and olfaction in the upper airway of the human. The airflow patterns obtained from these simulations should depict whether or not more particles travel through the olfactory region at a higher flow rate, indicating whether or not olfactory ability is increased. This thesis will detail the computational methodology which was used in order to obtain data, present the results which were found, and discuss conclusions of the study.

2.0 Computational Methodology

2.1 Standardized Nasal Cavity Geometry

The complex geometry of the human nasal cavity causes many challenges in a variety of fields – including nasal drug delivery, clinical research, respiratory physiology, and olfaction. To overcome these problems, a group at Carleton University created a standardized three-dimensional model of the human nose that is representative of the general population.

This standardized geometry was defined by aligning and processing 30 CT scans of human nasal cavities. The three measurements that were taken included the major axis of the nostril cross-section (length), minor axis of the nostril cross-section (width), and the angle of the major axis with the base of the nose (Liu et al., 2009). Left and right nasal cavities were separately analyzed to enhance the amount of data. Since the left and right nasal cavities are known to vary within a subject, this would truly create a larger data set, rather than creating duplicate geometries.

The present study began with an anatomically-correct standardized model of the right human nasal cavity, obtained from Liu et al. (2009). To correctly model inspired air from the external environment, the standardized model was merged with a reconstructed model of the external human head, based on the U.S. National Library of Medicine's Visible Human Dataset; this model can be seen in Figure 3.

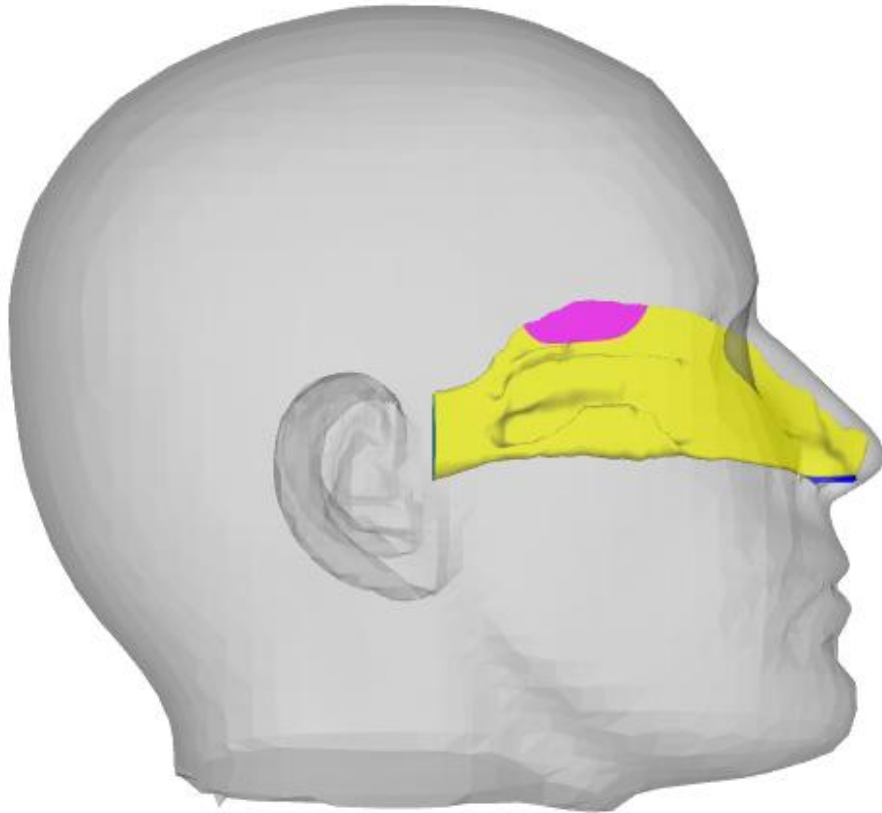


Figure 3: Merged model of the standardized nasal cavity (respiratory airway is yellow; olfactory airway is pink; vestibule is blue; nasopharynx is green) and the reconstructed human head.

2.2 Assumptions

The CFD calculation assumes that the bony internal structures of the human nasal cavity are rigid. Further, the influence of nostril motion is not expected to significantly affect the internal fluid dynamics and, thus, was not included as part of this study. The Womersley and Reynolds numbers were calculated using Equations (1) and (2) respectively. For the following equations, f is the sniff frequency (in Hz) Q^{peak} is the peak inspiratory airflow rate, ν is the kinematic viscosity of air, D_h is the hydraulic diameter of the airway, and A_c is the cross-sectional area of the airway.

$$Wo_{D_h} = \frac{D_h}{2} \sqrt{\frac{2\pi f}{\nu}} \quad (1)$$

$$Re_{D_h}^{\text{peak}} = \frac{Q^{\text{peak}} D_h}{A_c \nu} \quad (2)$$

The hydraulic diameter of the airway and cross-sectional area of the airway were measured from experimental data in this simulation. Human sniff frequency is approximately 0.5 Hz (Hornung, 2006) (Porter et al., 2007) and the peak flow rate during a sniff is about 700 ml/s (Hornung, 2006). Given these values and the other parameters, the Womersley and Reynolds numbers were calculated to be approximately 0.97 and 2000, respectively. A Womersley number of less than 1 indicates quasi-steady flow, while a Reynolds number of 2000 is generally considered to be at the high end of the laminar flow regime. Therefore, a laminar assumption can be made.

Finally, this study assumes that the mucus layer covering the majority of the nasal airways may be neglected. Due to the small relative thickness of the mucus layer compared with the dimensions of the nasal airways, the mucus layer has a negligible influence on the internal aerodynamics (Craven et al., 2007). Therefore, the walls can be assumed to be rigid and smooth.

2.3 Boundary Conditions

The left and right nasal cavities are completely separate. This allows only the right nasal airway to be modeled, and thus, only airflow in the right nasal airway is computed in this

study. The merged model of the human head and right nasal airway was placed in a large rectangular “box,” where farfield atmospheric pressure boundary conditions are specified. The size of the farfield computational boundary was made large enough to avoid inflow boundary effects on inspiratory airflow at the naris.

Since the nasal mucus layer has a negligible influence on the internal aerodynamics, no-slip boundary conditions were applied on all solid surfaces of the human nose and head. Nasopharynx and farfield pressure boundary conditions were specified such that the inspiratory airflow rate roughly matched the maximum sniff flow rate as defined by David Hornung (2006).

2.4 Grid Generation

Due to the complexity of the human nasal cavity geometry, an unstructured grid generation scheme was necessary. A semi-automated octree-based method (Harpoon, Sharc Ltd., Manchester, UK) was used to generate unstructured hexahedral grids by assigning separate surface cell sizes to different geometric parts based on the required grid refinement. An overall grid expansion ratio was also assigned to the grids. As a final step, smoothing iterations were performed to best improve grid quality.

The first step for grid generation was to split up the external geometry and nasal airway into multiple surface parts – including the head, nasal vestibule, respiratory airway, olfactory airway, and nasopharynx. This definition allowed for the regional specification of grid

resolution. A coarse-grid density may be used in the farfield, and then gradually refined closer to the head and nose. Fine-grid resolution is required in the main airway regions such as the respiratory and olfactory airways, while a slightly coarser grid may be used in the vestibule and nasopharynx.

Three different grids were generated – coarse, medium, and fine. The coarse grid contained 1.2×10^6 computational cells while the medium and fine grids contained 4.7×10^6 and 17.9×10^6 computational cells, respectively. A boundary layer mesh was applied to all three grids to better capture the near-wall velocity gradients. Additionally, a refinement region was specified around the nostril to better resolve the external fluid dynamics. The olfactory region was defined through reference to the Clinical Anatomy of the Nose, Nasal Cavity and Paranasal Sinuses (See Figure 161, Lang, 1989). Figure 4 shows a two-dimensional cross-section of a three-dimensional mesh, obtained from the fine mesh which was generated.

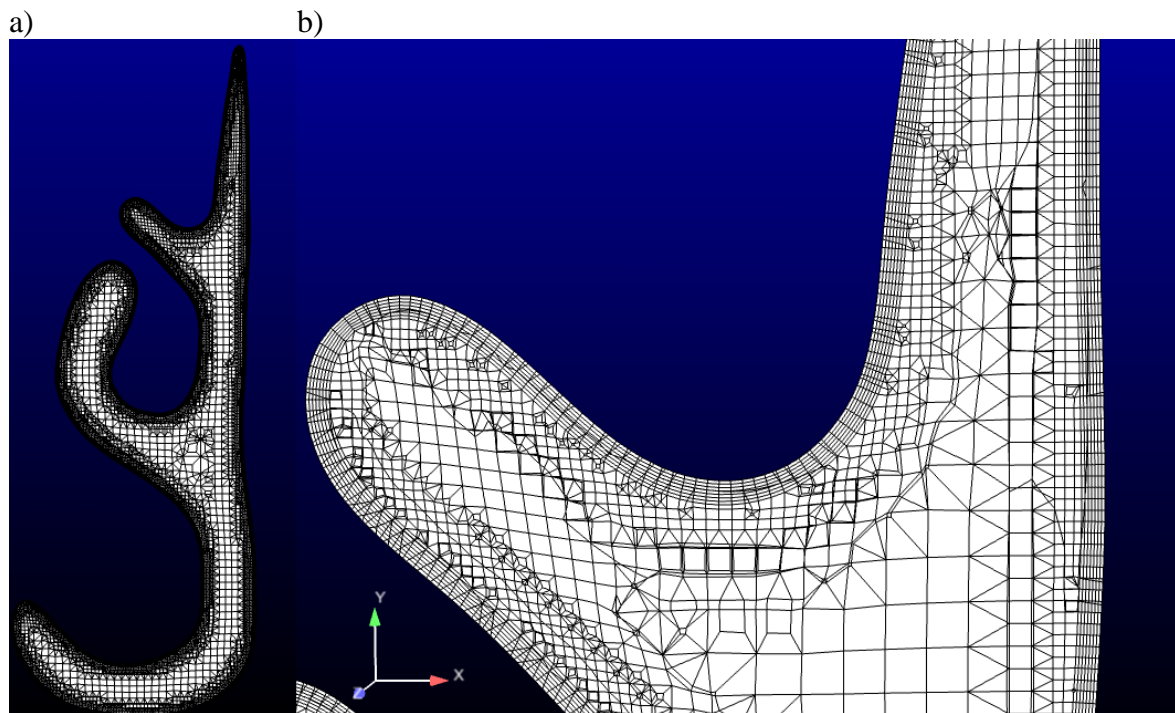


Figure 4: A 2-D cross-section of the 3-D fine mesh.

Figure 4(a) shows the entire cross section of the mesh, which is similar in geometry to Figure 1(b); however the cross-section in Figure 4(a) is of the right nasal cavity as opposed to the left nasal cavity as in Figure 1(b). Figure 4(b) zooms in on the region of the superior meatus in Figure 4(a) in order to better illustrate the grid refinement.

2.5 Numerical Methods

The commercial CFD code AcuSolve (ACUSIM Software, Inc., Mountain View, CA, USA) was used to numerically solve the incompressible Navier-Stokes equations on each computational mesh (coarse, medium, and fine). A second-order accurate finite element method was used to compute steady state solutions using an implicit Euler time integration scheme (see Craven et al., 2009 for more details). Computations were carried out on a parallel computer cluster at the Penn State Applied Research Laboratory, using 12, 16, and 20 processors for the coarse, medium, and fine mesh respectively.

3.0 Results and Discussion

The qualitative features of the CFD solutions were fairly consistent for the coarse, medium, and fine grids. The medium and fine grids resolved flow features in smaller areas more effectively than did the coarse grid. The overall flow patterns were remarkably similar regardless of the refinement of the grid, however there were marked differences in the flow rates and velocity profiles as the grid refinement progressed from coarse to fine.

As part of a CFD verification study, a Richardson extrapolation was performed. The theory behind the Richardson extrapolation requires that the calculated solutions fall within the asymptotic range of convergence as well as contain a “consistent” numerical method (Roache, 1998). For unstructured grids, which were used in this study, verification of global or integrated quantities is typically performed since direct comparison of nodal values requires interpolating the solutions to a common grid, introducing an additional source of error. In this study, the Richardson extrapolation was performed on the calculated airflow rates.

Equations (3)-(7) summarize the theory of Richardson extrapolation. For a “consistent” numerical method, the calculated solutions, $f_i(\Delta)$, better approximate the exact solution, f_{exact} , as the numerical error, $C\Delta_i^p$, decreases with grid refinement. Here, C is a coefficient, Δ is the grid spacing, and p is the observed order of convergence (Roache, 1998). Numerical solutions computed on the three grids – fine (f_1), medium (f_2), and coarse (f_3) – were used to evaluate p from Eq. (4) for a constant grid refinement ratio r , Eq. (5).

The estimated fractional error of the fine-grid solution, E_1 , was evaluated from Eq. (6), where the observed order of convergence p (Eq. (4)) was calculated, rather than using the theoretical convergence rate as is commonly done in two-grid convergence studies (Craven et al., 2009). The grid convergence index (GCI), originally proposed by Roache and defined in Eq. (7), is a measure of the fractional error that has a high probability of bounding the actual error of the numerical solution (Roache, 1998). Based on the recommendation of Roache (Roache, 1998) a “factor of safety,” F_s , of 1.25 was used in the present grid convergence study, where solutions from the three different grids are utilized to determine the observed order of convergence, p .

$$f_i(\Delta) = f_{\text{exact}} + C\Delta_i^p \quad (3)$$

$$p = \frac{\ln\left(\frac{f_3 - f_2}{f_2 - f_1}\right)}{\ln(r)} \quad (4)$$

$$r \approx \left(\frac{N_1}{N_2}\right)^{1/3} \approx \left(\frac{N_2}{N_3}\right)^{1/3} \quad (5)$$

$$E_1 = \frac{\left(\frac{f_2 - f_1}{f_1}\right)}{r^p - 1} \quad (6)$$

$$GCI_1 = F_s |E_1| \quad (7)$$

In the present study, the flow rates were averaged for time steps 30 through 45, after the solution had reached a quasi-steady state. The flow rates for each grid and time step can be seen in Figure 5. The Richardson extrapolation, performed on the averaged flow rates, yields

$p = 3.48$, $E_1 = -0.32\%$ and $GCI_1 = 0.40\%$ where E_1 and GCI_1 are for the fine-grid solution. The grid refinement ratio was 1.56, as the fine, medium, and coarse grids had 17.9, 4.7 and 1.2 million cells, respectively.

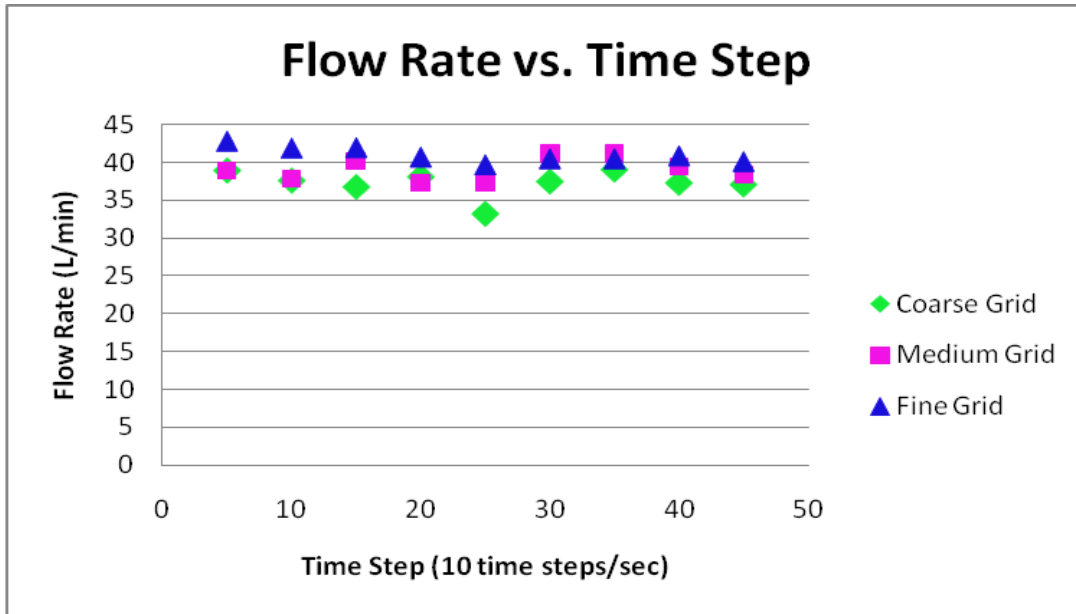


Figure 5: Computed flow rates through the human nasal cavity as a function of time step.

The peak flow rate through the human nasal cavity during sniffing is 40 L/min (Hornung, 2006). Consequently, a flow rate of 40 L/min was used in this work to study the fluid dynamics at a physiologically-realistic flow rate. Figures 6-12 show coronal-plane velocity contours for the right human nasal cavity. Figure 6 begins with coronal-plane cross-section of the anterior portion of the naris; each cross-section moves toward the posterior end of the nasal cavity in 2 mm increments. The final cross-section in Figure 12 is the nasopharynx, where the nasal airway bends 90 degrees and descends through the pharynx to the trachea and lungs. As can be seen in these figures, the highest velocities occur in the nasal valve and the middle of the airways. This is contrary to previous experiments that considered restful

breathing at lower flow rates and found the highest velocities to be in the nasal valve and inferior airways, and may be due to the higher flow rate. The olfactory region is located in the superior portion of coronal-plane cross-sections 30-42 (Figures 10-11), as determined by the anatomy shown previously in Figure 2. This region experiences a relatively low velocity under the given conditions. This lower velocity magnitude may enhance odorant deposition in this region of the nasal cavity, which would be ideal for olfaction. Higher velocities in the olfactory region may have an adverse effect on odorant deposition efficiency, which would hinder olfactory function. However, odorant transport simulations are required to further investigate such phenomena.

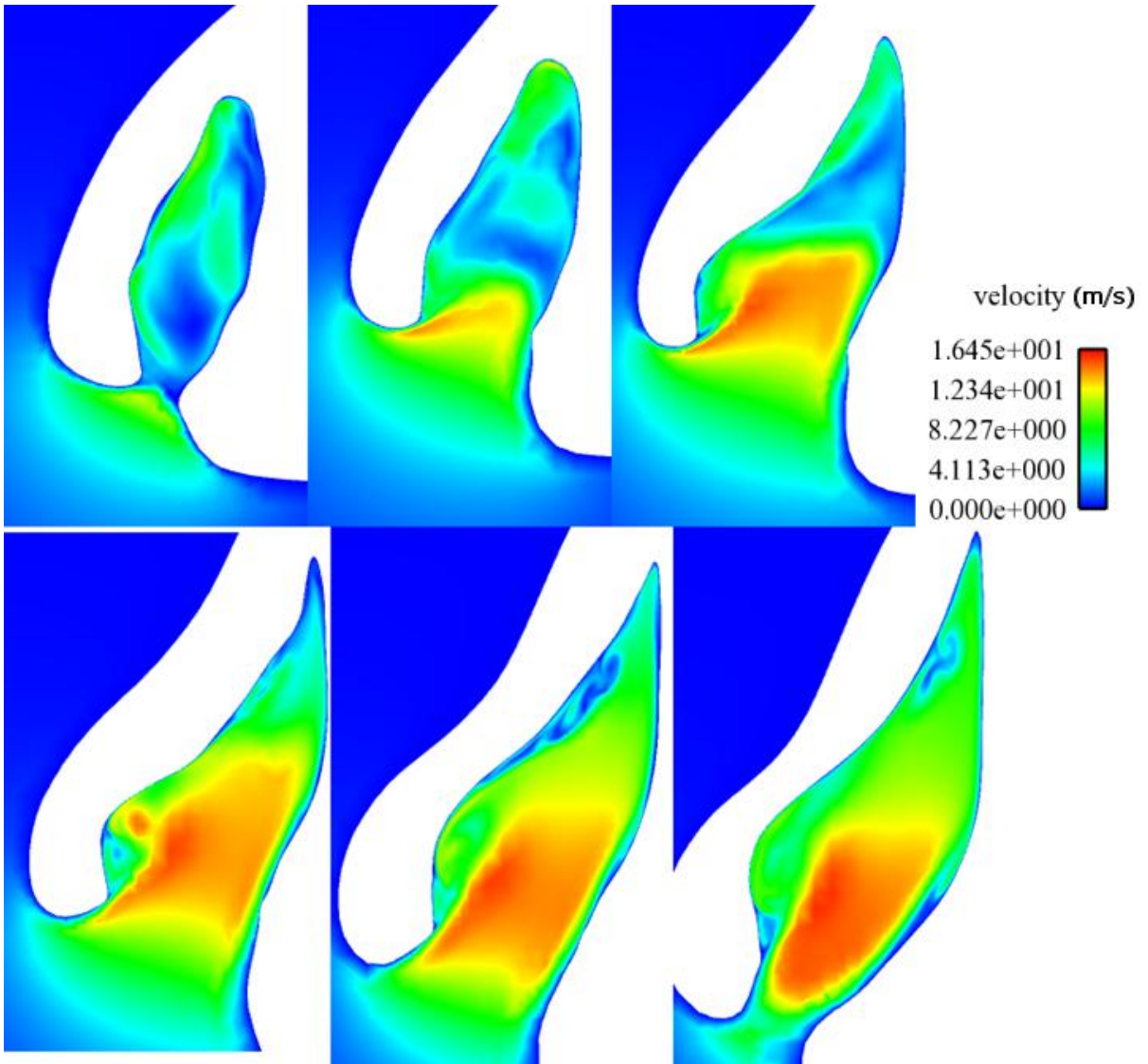


Figure 6: Velocity contours at cross-sections 1-6 through the human nasal cavity at a flow rate of 40 L/min. Cross-section one is at the anterior tip of the naris.

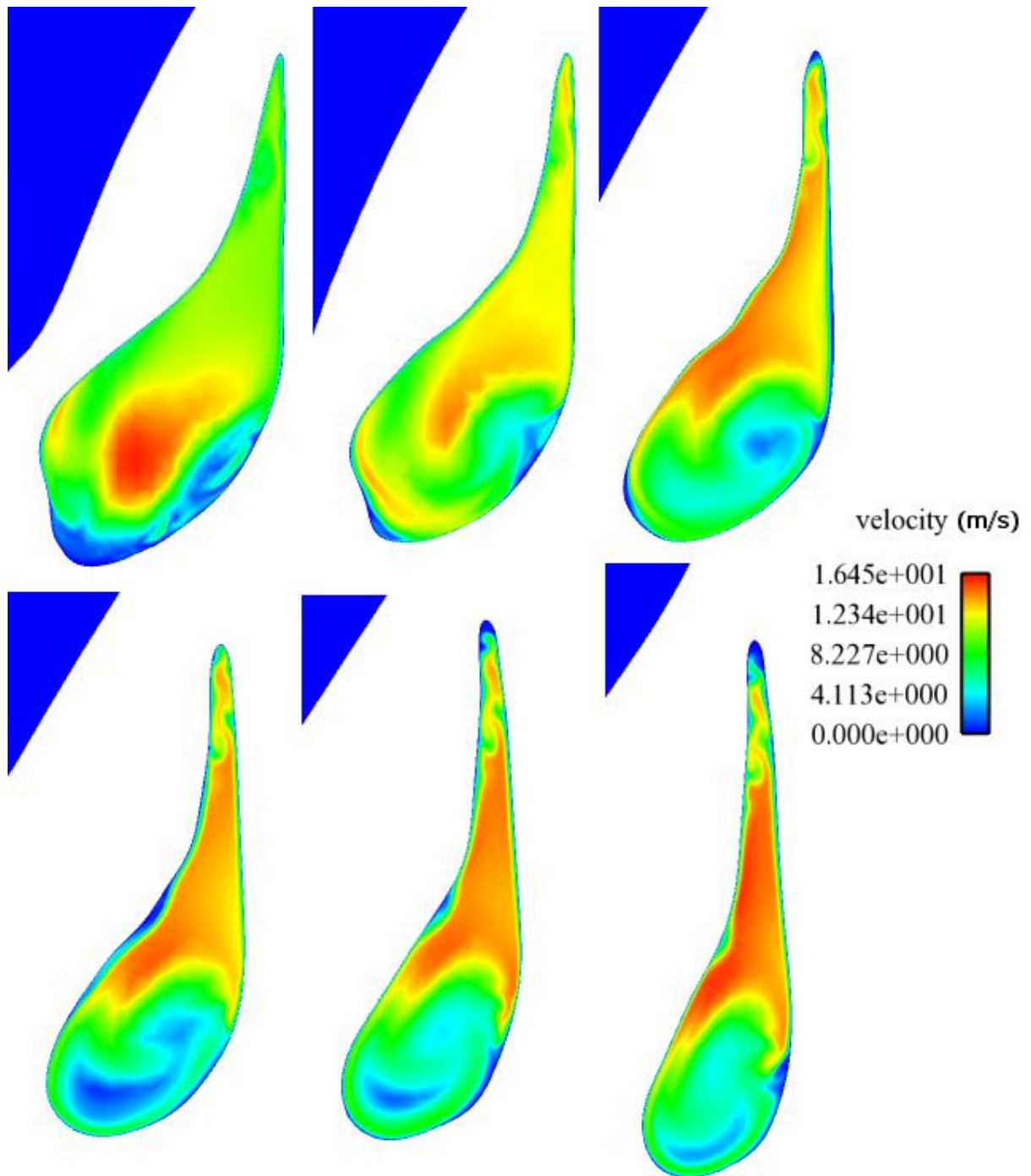


Figure 7: Velocity contours at cross-sections 7-12 through the human nasal cavity at a flow rate of 40 L/min.

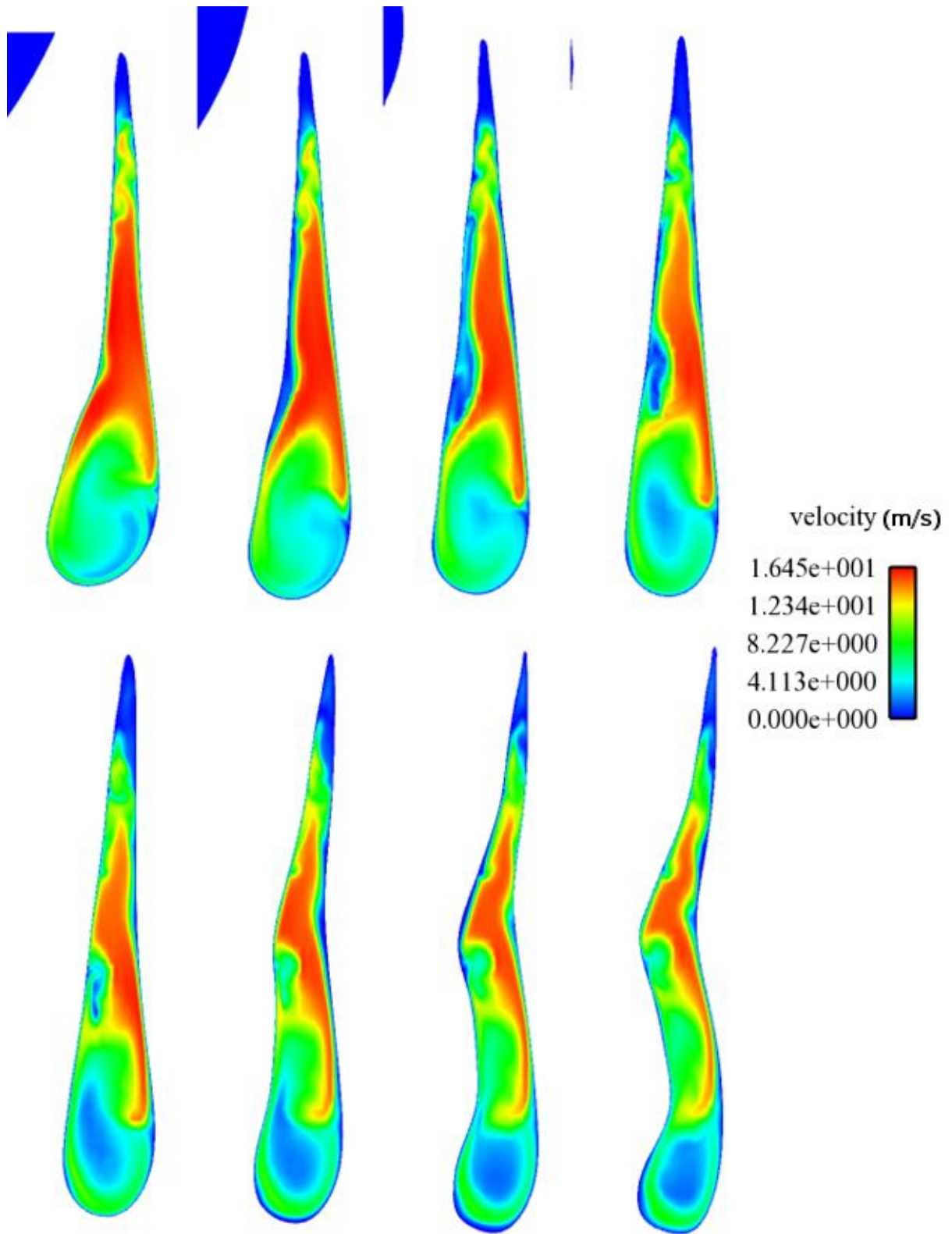


Figure 8: Velocity contours at cross-sections 13-20 through the human nasal cavity at a flow rate of 40 L/min.

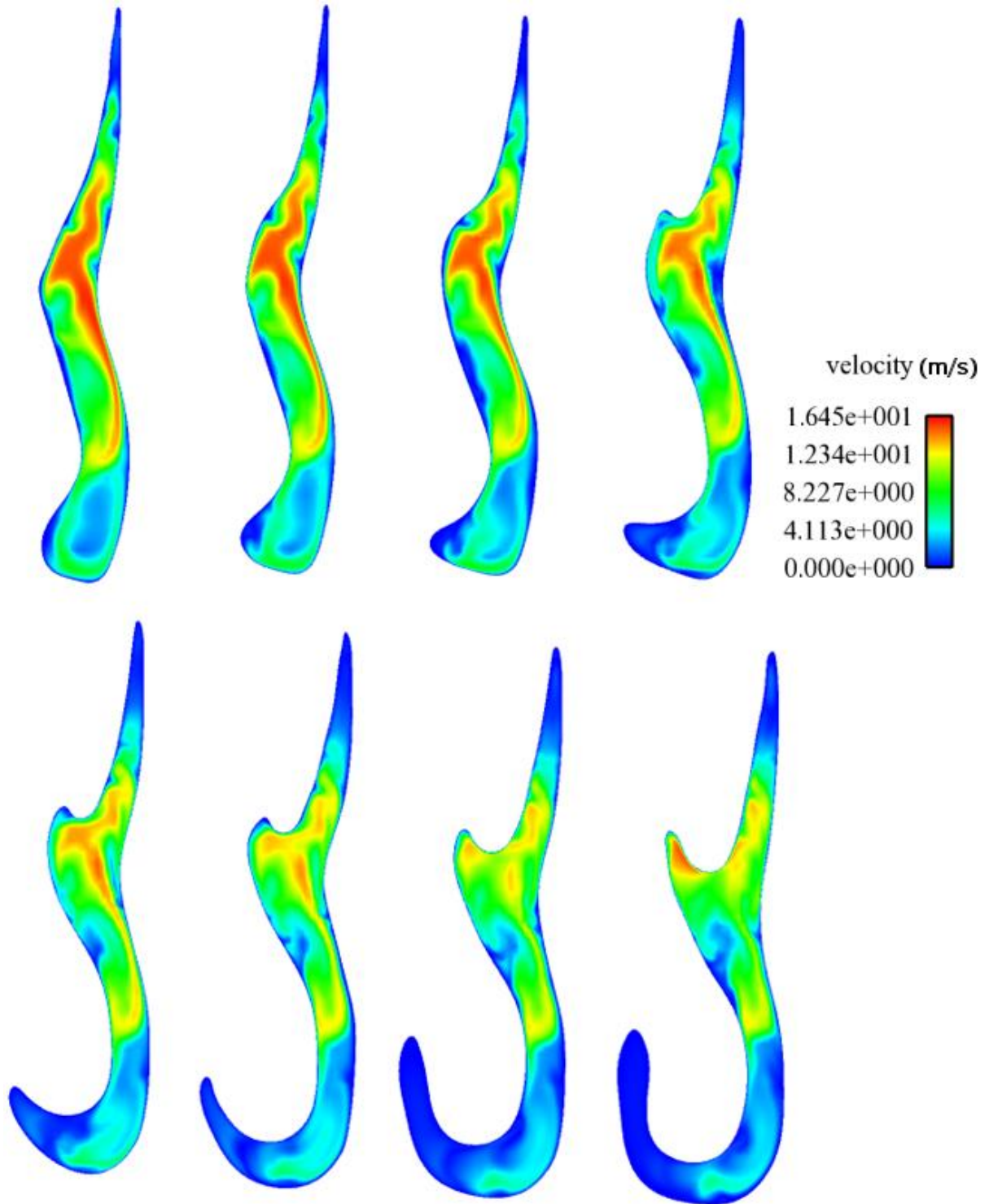


Figure 9: Velocity contours at cross-sections 21-28 through the human nasal cavity at a flow rate of 40 L/min.

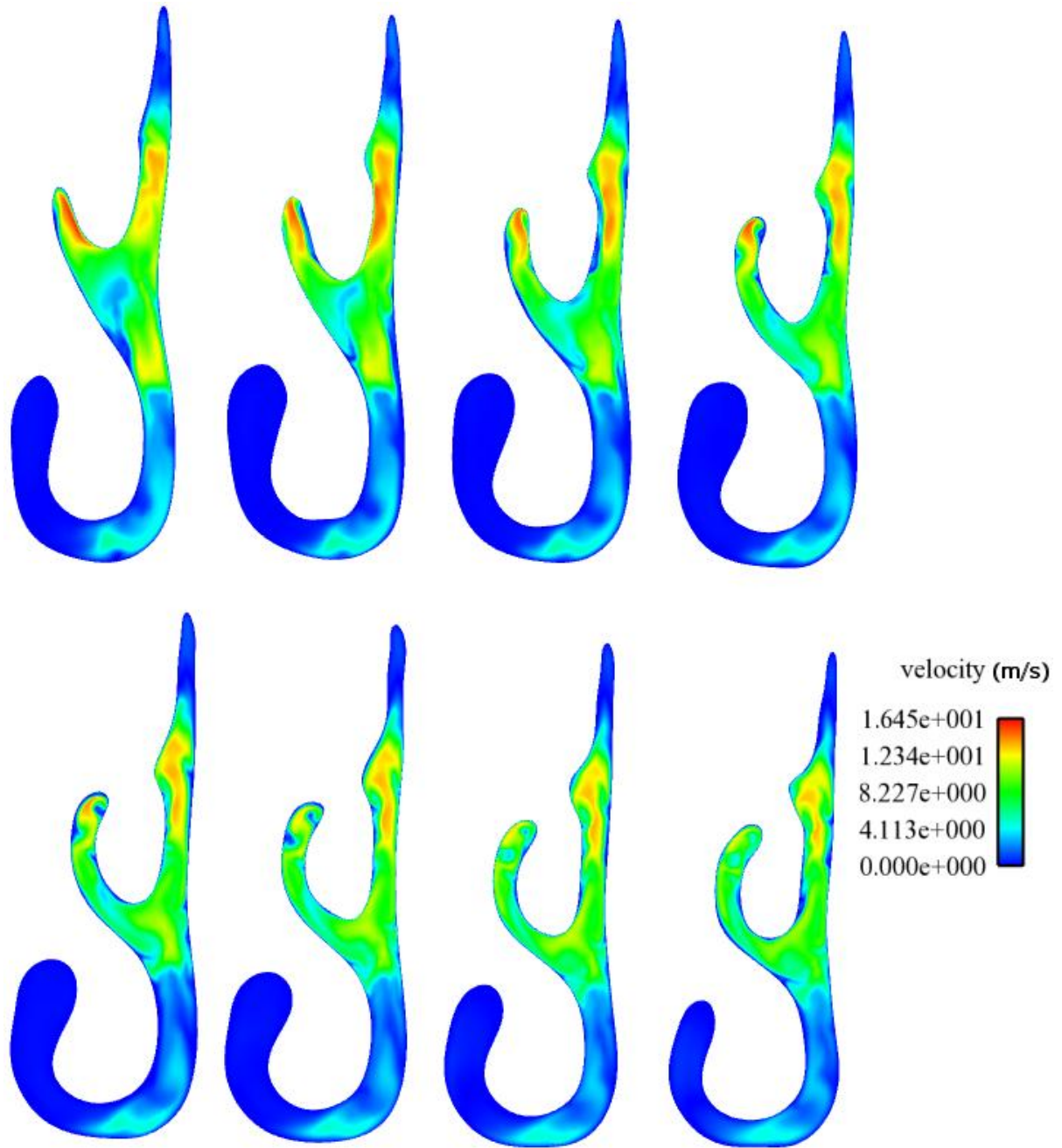


Figure 10: Velocity contours at cross-sections 29-36 through the human nasal cavity at a flow rate of 40 L/min. The olfactory region begins in coronal cross-section 30.

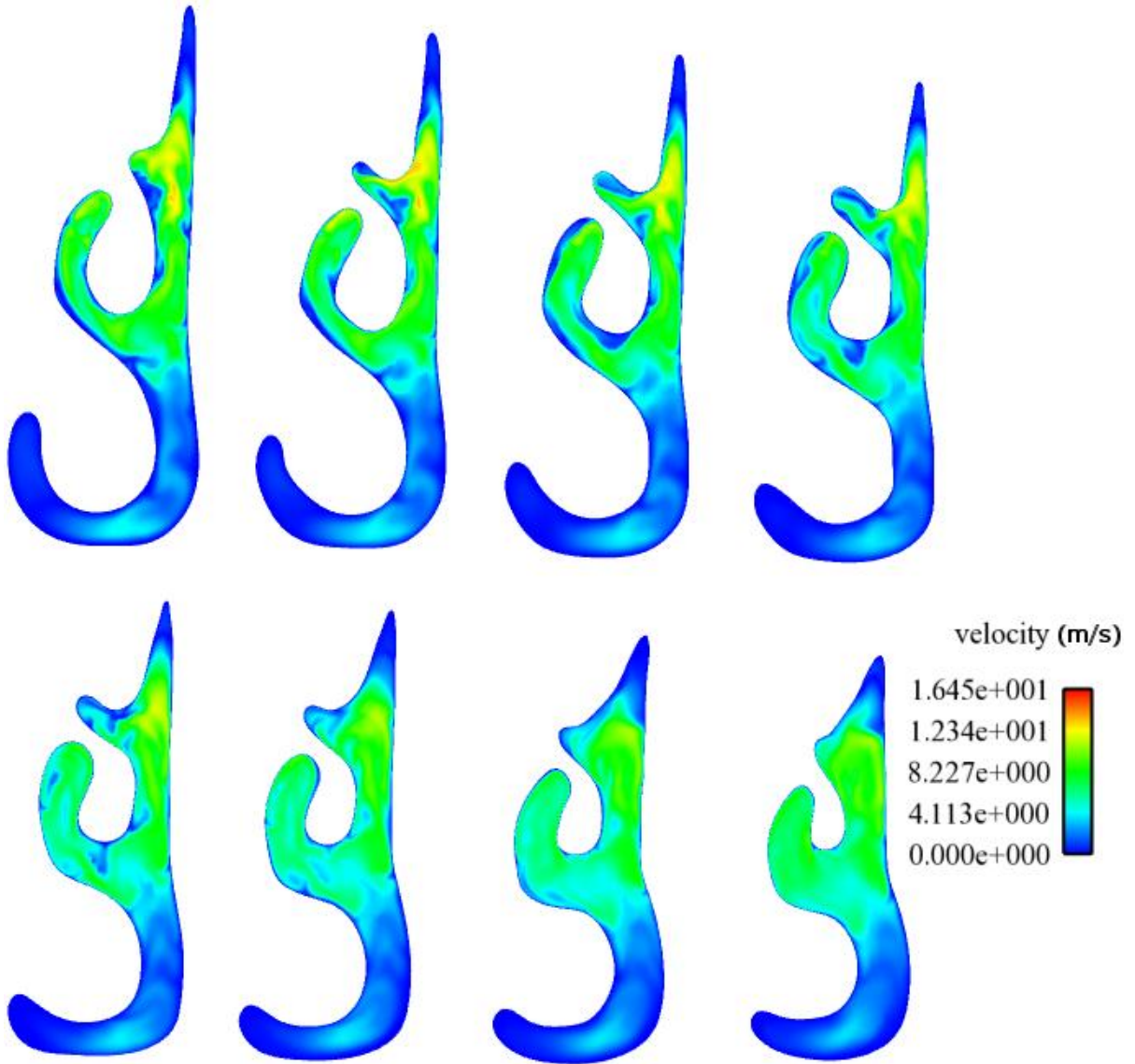


Figure 11: Velocity contours at cross-sections 37-44 through the human nasal cavity at a flow rate of 40 L/min. The olfactory region ends in coronal cross-section 42.

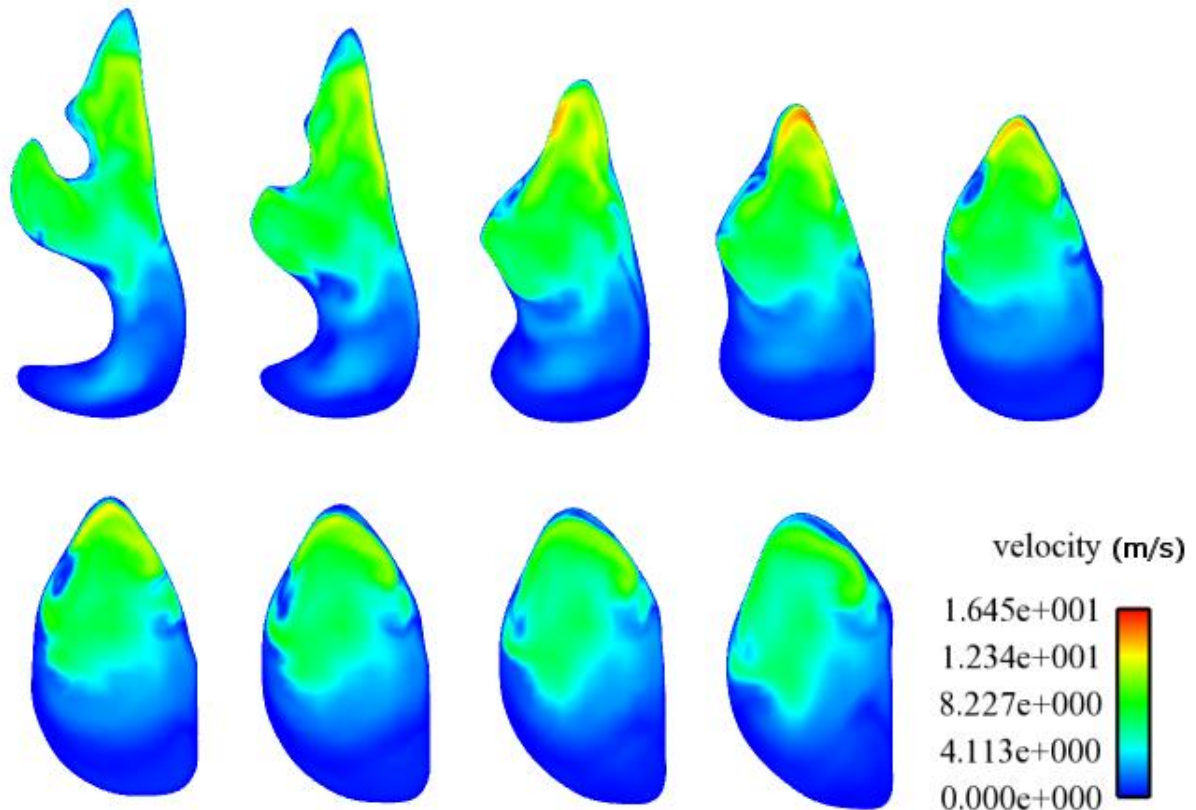


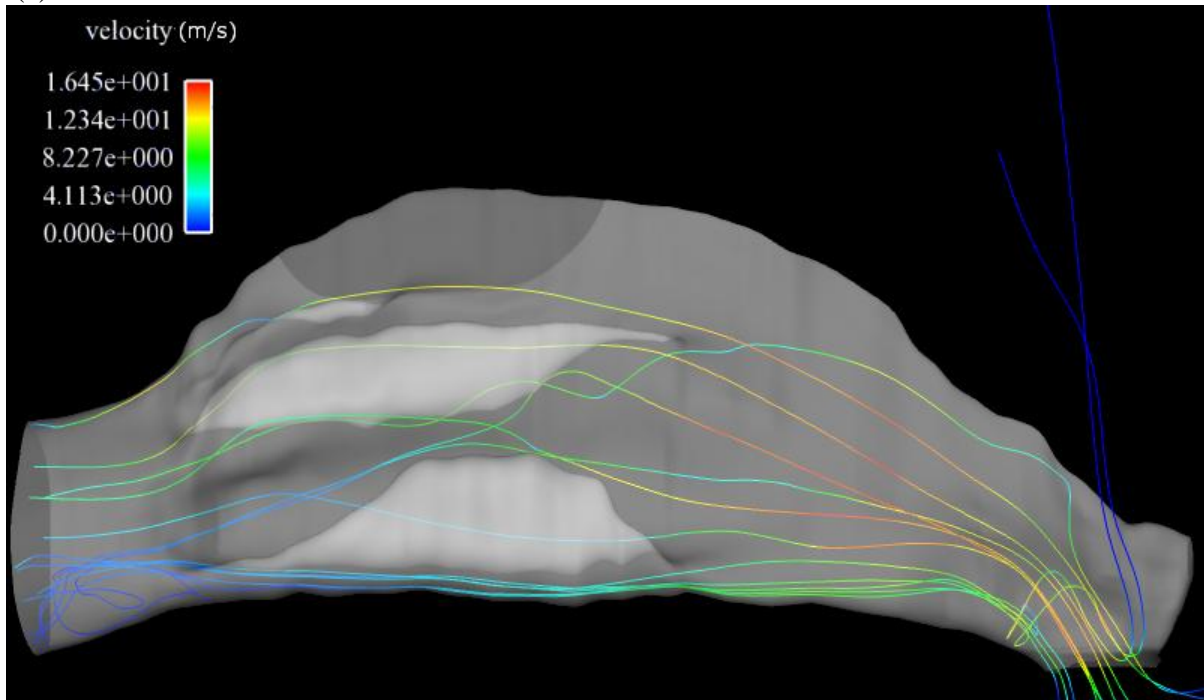
Figure 12: Velocity contours at cross-sections 45-53 through the human nasal cavity at a flow rate of 40 L/min. The final coronal cross-section, 53, is the nasopharynx.

Airflow patterns in the human nasal cavity during sniffing can best be seen in Figure 13, which shows streamlines of neutrally-buoyant particles. The streamlines travel from the external environment, into the naris, then through the nasal cavity until finally passing through the nasopharynx. Both Figures 13(a) and 13(b) reveal the airflow patterns through the right human nasal cavity. The olfactory region is the darker gray area in the superior portion of the nasal cavity. Only a small percentage of the air in the human nasal cavity flows through the olfactory region, which is similar to the results which have been obtained previously for resting breathing flow rates. The streamlines that do travel through the olfactory region of the nasal cavity generally enter the nose through the anterior portion of

the naris, as is expected; however, not all particles entering the nasal cavity via the anterior section of the naris reach the olfactory region. Generally, those streamlines that enter the anterior part of the naris travel through the superior part of the nasal cavity and those streamlines that enter the posterior part of the naris travel through the inferior section of the nasal cavity.

Additionally, there are a couple of small regions where there is flow separation. The first can be seen in the nasopharynx, in both Figure 13(a) and 13(b). This is caused by the expansion of the nasopharynx as the air flows toward the back of the nasal cavity. The second region which shows flow separation is the vestibule; this can be seen in Figure 13(b). This flow separation is also due to the sudden expansion of the nasal cavity.

(a)



(b)

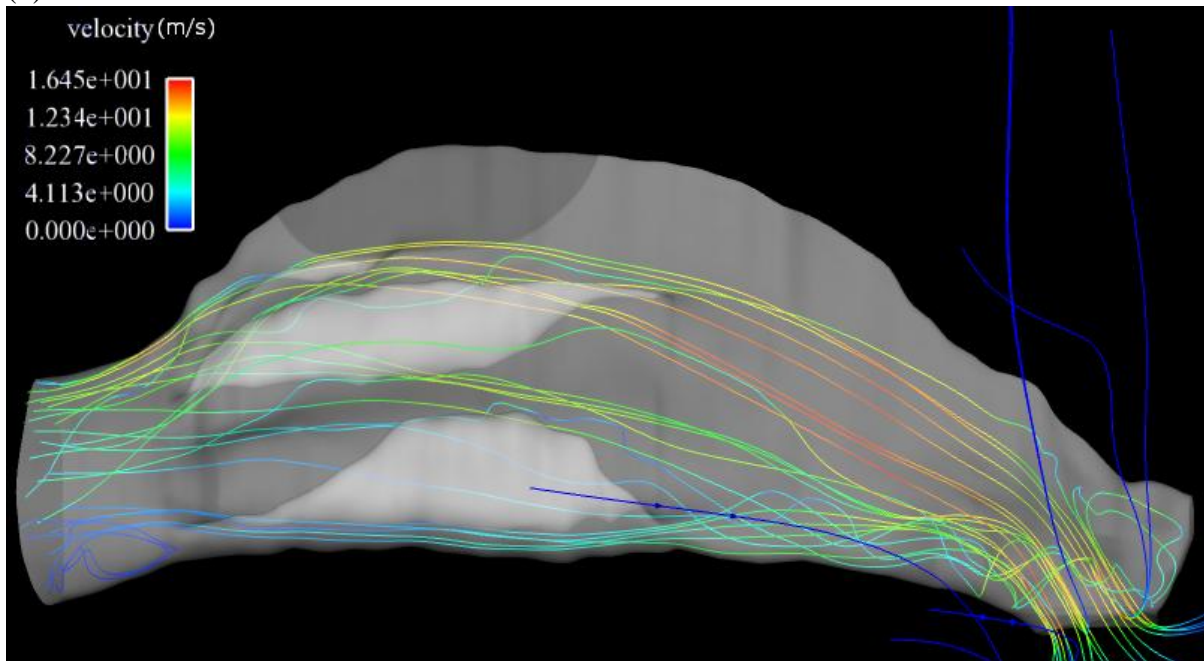
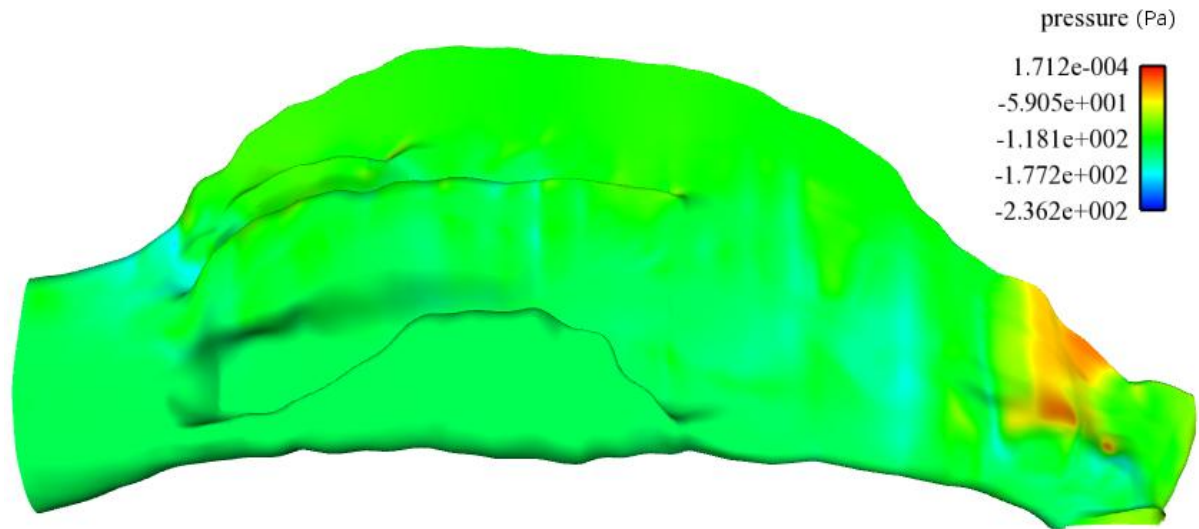


Figure 13: Streamlines of neutrally-buoyant particles through the human nasal cavity at a flow rate of 40 L/min.

The pressure distribution within the nasal cavity can be seen in Figure 14. The highest pressure occurs near the nasal bone boundary and vestibule, while the rest of the nasal cavity has a fairly constant pressure. Despite the pressure being fairly constant, the areas of the nasal cavity which have a higher velocity of air flowing through them display a slightly lower pressure than those which contain lower airflow. There is a high pressure in the vestibule due to the airflow impinging as it accelerates through the nasal valve.

(a)



(b)

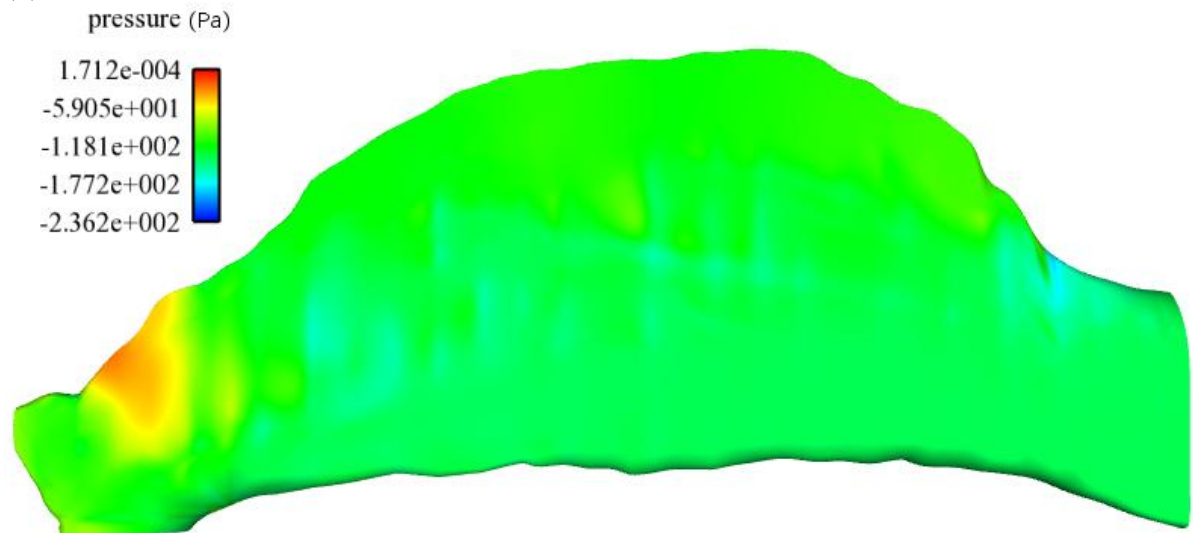


Figure 14: Surface pressure contours in the right human nasal cavity for a flow rate of 40 L/min.

4.0 Conclusions

A CFD model of a standardized human nasal airway was developed that required at least 1.2×10^6 computational cells. To perform a verification study and analyze the airflow patterns in the nasal airway, CFD grids containing up to approximately 18×10^6 computational cells were developed.

Qualitatively, the coarse, medium, and fine grids all showed the same patterns of airflow through the human nasal cavity. Quantitatively, a more refined grid better captured the flow structures, especially in smaller portions of the nasal cavity. A Richardson extrapolation was performed to determine the inherent numerical error present in the “fine” grid solution during sniffing, which showed acceptable numerical accuracy (<1% error).

The high flow rate (40 L/min) that was simulated here did not appear to facilitate the transport of more odorant molecules through the olfactory region of the human nasal cavity, compared with other studies at lower airflow rates (Keyhani et al., 1997) (Hahn et al., 1993) (Taylor et al., 2009). The flow patterns through the human nasal cavity were such that a relatively small portion of the airflow entering the naris actually traveled through the olfactory region, which is similar to that reported in previous studies at lower flow rates during resting breathing.

The speed of the air flowing through the olfactory region is much slower than that of the air that flows through the middle portion of the nasal cavity. This likely facilitates the

deposition of odorant molecules onto the olfactory epithelium, where olfactory sensation occurs. Compared with other studies of human nasal airflow at resting breathing flow rates (Keyhani et al., 1997) (Hahn et al., 1993) (Taylor et al., 2009), the results from this study do not appear to show any significant benefits to sniffing related to human olfactory ability.

4.1 Future Work

Future studies should consider the potential influence of transitional and turbulent flow on nasal airflow patterns and olfaction in humans, since the Reynolds number was at the high end of the laminar flow regime. Additionally, calculations of resting breathing flow rates should be performed using the standardized human nasal cavity used in this study in order to compare them directly with the results presented in this thesis for higher sniffing flow rates. Finally, it would be interesting to simulate retronasal airflow patterns, and compare them with the orthonasal airflow results which were presented in this thesis.

References

Bisulco, S. and B. Slotnick. Olfactory discrimination of short chain fatty acids in rats with large bilateral lesions of the olfactory bulbs. *Chemical Senses*, 28: 361-370.

Craven, B.A., T. Neuberger, E.G. Paterson, A.G. Webb, E.M. Josephson, E.E. Morrison, and G.S. Settles. Reconstruction and Morphometric Analysis of the Nasal Airway of the Dog (*Canis familiaris*) and Implications Regarding Olfactory Airflow. *The Anatomical Record*, 290: 1325-1340, 2007.

Craven, B.A., E.G. Paterson, and G.S. Settles. The fluid dynamics of canine olfaction: a new explanation for macrosmia. *Journal of the Royal Society Interface*, published online before print December 9, 2009
<http://rsif.royalsocietypublishing.org/content/early/2009/12/09/rsif.2009.0490>.

Doorly, D.J., D.J. Taylor, A.M. Gambaruto, R.C. Schroter, and N. Tolley. Nasal architecture: form and flow. *Philosophical Transactions of the Royal Society A*, 366:3225–3246, 2008.

Elad, David, Michael Wolf, and Tilman Keck. Air-conditioning in the human nasal cavity. *Respiratory Physiology & Neurobiology*, 163:121–127, 2008.

Garcia, Guilherme, Neil Bailie, Dario Martins, and Julia Kimbell. Atrophic rhinitis: a CFD study of air conditioning in the nasal cavity. *Translational Physiology*, 103:1082–1092, 2007.

Glusman, G., I. Yanai, I. Rubin, and D. Lancet. The complete human olfactory subgenome. *Genome Research*, 11: 685-702, 2001.

Hornung, David. Nasal Anatomy and the Sense of Smell. *Taste and Smell: An Update*. Karger: New York, 2006.

Hahn, I., P.W. Scherer, and M.M. Mozell. Velocity profiles measured for airflow through a large-scale model of the human nasal cavity. *Modeling Physiology*, 75: 2273-2287, 1993.

Kelly, J.T., A.K. Prasad, and A.S. Wexler. Detailed flow patterns in the nasal cavity. *Journal of Applied Physiology*, 89:323–337, 2000.

Keyhani, K., P.W. Scherer, and M.M. Mozell. Numerical simulation of airflow in the human nasal cavity. *Journal of Biomechanical Engineering*, 117:429–441, 1995.

Keyhani, K., P.W. Scherer, and M.M. Mozell. A numerical model of nasal odorant transport for the analysis of human olfaction. *Journal of Theoretical Biology*, 186:279–301, 1997.

Lang, J. *Clinical Anatomy of the Nose, Nasal Cavity and Paranasal Sinuses*. Thieme Medical Publishers: New York, 1989.

Liu, Y., M.R. Johnson, E.A. Matida, S. Kherani, and J. Marsan. Creation of a standardized geometry of the human nasal cavity. *Journal of Applied Physiology*, 106:784–795, 2009.

Liu, Y., E.A. Matida, J. Gu, and M.R. Johnson. Numerical simulation of aerosol deposition in a 3-d human nasal cavity using rans, rans/eim, and les. *Journal of Aerosol Science*, 38:683–700, 2007.

Laska, M., A. Seibt, and A. Weber. “Microsmatic” primates revisited: Olfactory sensitivity in the squirrel monkey. *Chemical Senses*, 25: 47-53, 2000.

Porter, J., B. Craven, R.M. Khan, S. Chang, I. Kang, B. Judkewicz, J. Volpe, G. Settles, and N. Sobel. Mechanisms of scent-tracking in humans. *Nature Neuroscience*, 10: 27-29, 2007.

Roache, P.J. *Verification and Validation in Computational Science and Engineering*. Hermosa: Albuquerque, 1998.

Shepherd, G.M. The human sense of smell: Are we better than we think? *PLoS Biology*, 2:0572–0575, 2004.

Shi, H., C. Kleinstreuer, and Z. Zhang. Laminar airflow and nanoparticle or vapor deposition in a human nasal cavity model. *Journal of Biomechanical Engineering*, 128:697–706, 2006.

Subramaniam, R.P., R.B. Richardson, K.T. Morgan, J.S. Kimbell, and R.A. Guilmette. Computational fluid dynamics simulations of inspiratory airflow in the human nose and nasopharynx. *Inhalation Toxicology*, 10:473–502, 1998.

Taylor, D.J., D.J. Doorly, and R.C. Schroter. Inflow boundary profile prescription for numerical simulation of nasal airflow. *Journal of the Royal Society Interface*, 2009.

Weinhold, I. and G. Mlynski. Numerical simulation of airflow in the human nose. *Rhinology*, 261:452–455, 2004.

Zhao, K. and P. Dalton. The way the wind blows: Implications of modeling nasal airflow. *Rhinitis*, 7:117–125, 2007.

Zhao, K., P. Dalton, G.C. Yang, and P.W. Scherer. Numerical modeling of turbulent and laminar airflow and odorant transport during sniffing in the human and rat nose. *Chemical Senses*, 31:107–118, 2006.

Zozulya, S., F. Echeverri, and T. Nguyen. The human olfactory receptor repertoire. *Genome Biology*, 2: RESEARCH0018, 2001.

Zhao, K., P.W. Scherer, S.A. Hajiloo, and P. Dalton. Effect of anatomy on human nasal air flow and odorant transport patterns: Implications for olfaction. *Chemical Senses*, 29:365–379, 2004.

Acknowledgments

Dr. Brent Craven, special thanks

The Garfield Thomas Water Tunnel and Applied Research Laboratory, Penn State University

Dr. William Hancock

The Schreyer Honors College, Penn State University

Academic Vita of Elizabeth M. Shenk

Name: Elizabeth Shenk

Permanent Address:

9 Meadowview Ct.
Lewisburg, PA 17837

Education:

Major: Bioengineering
Honors: Bioengineering

Thesis Title: A computational study of airflow in a standardized human nasal cavity:
implications regarding olfaction

Thesis Advisor: Brent A. Craven

Work Experience:

August 2009 – May 2010
Student Intern

Simulated airflow through the respiratory and olfactory systems using CFD
Applied Research Lab, Penn State University, University Park, PA 16802
Dr. Brent A. Craven

June 2009 – August 2009

Research Intern

Performed genetic research applying the results to abdominal aortic aneurysm risk
Weis Center for Research, Geisinger Medical Center, Danville, PA 17821
Dr. David J. Carey

Awards:

Dean's List, all semesters
President's Freshman Award

Memberships:

Society of Women Engineers
National Society of Collegiate Scholars
Golden Key International Honour Society

Community Involvement:

Member of Grace Lutheran Church Choir
Small Group Leader for Lutheran Allegheny Synod Senior High Youth Event
(2008, 2009)

International Education:

Summer 2008 at University of Sussex in Brighton, England